Image processing applied to tribological dry contact analysis

Alizée Bouchot, Amandine Ferrieux, Johan Debayle, Guilhem Mollon, Sylvie Descartes

Version of Record: https://www.sciencedirect.com/science/article/pii/S004316482100137X
Manuscript_193bc5b00a94fe737fbf4728295a87cf

Image Processing applied to tribological dry contact analysis

Alizée Bouchot[1], Amandine Ferrieux[1], Johan Debayle[2], Guilhem Mollon[1], and Sylvie Descartes[1]

[1] Univ Lyon, INSA-Lyon, CNRS UMR5259, LaMCoS, F-69621, France.
[2] Mines Saint-Etienne, CNRS UMR 5307, LGF, Centre SPIN, 158 cours Fauriel, F-42023 Saint-Etienne Cedex 2, France
*Corresponding authors: sylvie.descartes@insa-lyon.fr
alizee.bouchot@insa-lyon.fr

The prediction of dry friction requires a quantification of the rheology of the tribological interface (third body). Until now this rheology has been characterized qualitatively by a broad description of its morphology (from powdery granular media to ductile continuous media) at the contact scale. The present work proposes to enrich this characterization through advanced image processing. Four steps are followed: pin-on-disk experiments, image acquisition of particles, image processing, and extraction of quantitative characteristics of third body particles. “Classical” descriptors (circularity, length, perimeter), and new relevant descriptors are studied, in order to consider the whole diversity of third body constituent’s layout and features. These descriptors are either contour- or texture-related [1]. This approach provides promising results. A future integration of these descriptors in machine learning algorithms [2] might allow a better understanding of the mechanisms involved in dry contacts.

Keywords: tribology, third body, dry friction, image processing

1. Introduction

The interest in the study of surfaces is fairly recent and was theorized by Peter Jost in 1966 [3], following a study highlighting the costs caused by wear and friction in general economy. Following this, numerous studies and theories were developed, notably the theory of the third body [4]. It is based on the study of the flows of matter present in the contact and was then formalized through the concept of tribological circuit by Berthier [5]. The different stages of a dry contact’s life can usually be well interpreted by adopting this perspective. However, this operation is very subjective and relies on the expertise of the tribologist. This is why many studies have been devoted to the use of image analysis to study and characterize the wear particles [6] and thus relate their properties to the physical phenomena specific to contact, and more specifically to wear. Roylance et al. proposed a correspondence between wear characteristics and particle properties [7], in particular the morphology that would provide information on rate, source and type of wear. Following such an approach, the study of wear particles by image analysis may give access to their shape and size properties [8] and make it possible to understand what type of wear is at work. Typical applications could be found in maintenance of industrial machinery, for example. In most studies, wear particles are collected and observed thanks to microscopy (optical or electronic). Then the images undergo processing such as filter application and contrast modification, in order to be segmented by various techniques [9]. Morphological properties are then extracted from binary images and can therefore be processed either manually or automatically [10]. In the context of lubricated contacts, the particles are collected by ferrography, and can then be studied individually on a uniform background. We however restrict this study to dry friction.

While many studies are conducted in an industrial context or with the will to reproduce the industrial conditions, the present study wishes to continue the work reported in Jaza et al. [2] and remains very academic in its spirit. The main idea of this work was to use Machine Learning (ML) to build a logical connection between the morphologies of the third body particles (described by a limited number of geometrical descriptors) and the rheology of the interface. The term rheology had in this context a very general definition: it could be defined as the characterization of the transformation and evolution of the third body. The same terminology is adopted in the present paper. The ML algorithm developed in the study of Jaza et al. achieved only moderate success rates, and this was attributed to severe limitations in the morphological and rheological databases that were built from the experimental campaign. It was concluded that an enrichment of these databases by more appropriate geometrical descriptors might allow better

performance in predicting rheology from morphology. The present study aims to bring such improvement.

Third body particles are produced with a pin-on-disk tribometer, which is presented in the next section. They are studied without being collected from the disk. For this purpose, a scanning electron microscope is used to acquire images, then an image analysis program developed in python language is developed to extract relevant quantitative information about the morphology of wear particles.

2. Experimental methods

2.1. Materials

The first bodies are made of 35CrNiMo16 (DIN/EN), a low alloy steel, whose chemical and mechanical properties are presented in table 1 and 2. This material is highly used in the manufacturing of highly stressed parts regardless of their dimensions across different industrial fields, thanks to its high hardenability and important impact strength level. In the present case, it was chosen for its ability to generate a sufficient amount of wear debris.

Table 1: Chemical composition of 35CrNiMo16 steel

C (%)	**Mn (%)**	**Si (%)**	**Ni (%)**	**Cr (%)**	**Mo (%)**	**S (%)**
0,32 – 0,39	0,50 – 0,80	0,10 – 0,40	3,60 – 4,10	1,60 – 2,00	0,25 – 0,45	≤0,025

Table 2: Mechanical properties of 35CrNiMo16 steel

E (MPa)	**ν**	**$Rp_{0,2\%}$ (MPa)**	**Rm (MPa)**	**Hardness**
205 000	0,3	0,10 – 0,40	3,60 – 4,10	50 HRC

The experiments are performed on a pin-on-disk tribometer. The pins are machined with a radius of curvature of 5 mm ± 0.80. For each test a new pin is used. Two types of disc surfaces are used, one with parallel striations to the sliding direction and one with perpendicular striation to the sliding direction, which are assigned the designations of $D_{//}$ and $D_{\perp}$, respectively. Initial surfaces and surface morphologies of the wear tracks and counterfaces are extracted using a Altimet non-contact optical profiler (Fig. 1). Prior to analyses and sliding tests, the as-received samples surfaces are cleaned by ultrasound and chemically in an ethyl acetate bath for 5 min. This cleaning eliminates residual pollution due to specimen handling and machining. Then rinsing is done in an ethanol bath for 5 min.

The root mean square roughness of the initial surfaces is S_a = 1.62 µm and R_a = 0.421 µm for disk $D_{//}$ and S_a = 2.11 µm and R_a = 0.6 µm for disk $D_{\perp}$

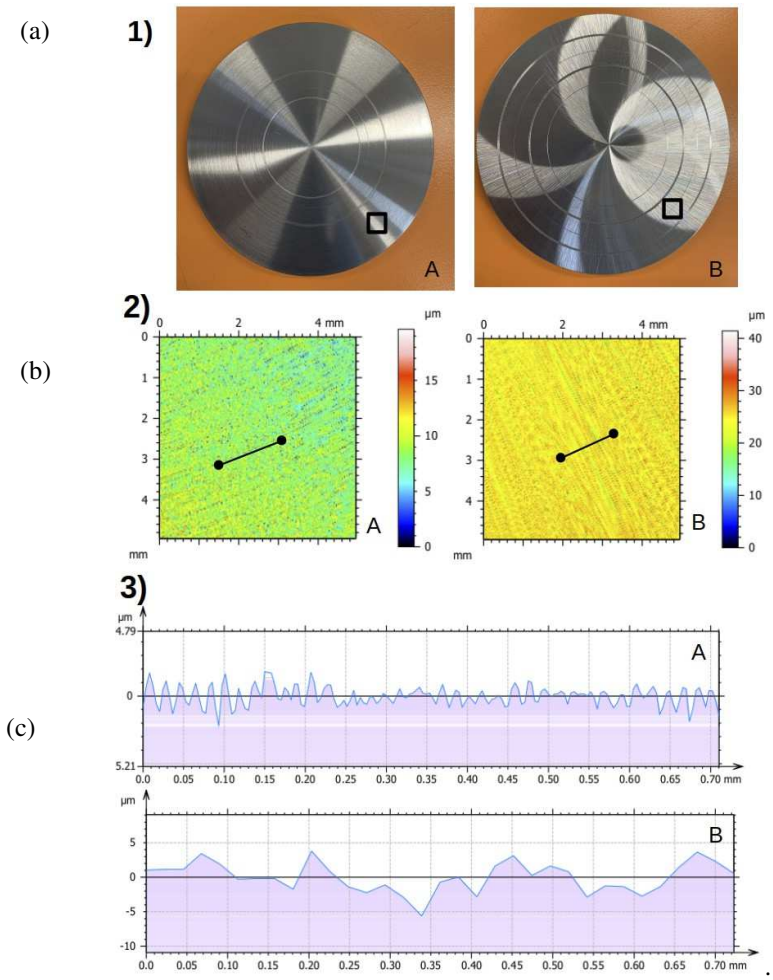

Figure 1: Initial discs surfaces, (A) Disk D// and (B) Disk D⊥: (a) Macro views, (b) 3D topography, (c) cross-section profiles along the sliding direction.

2.2. Sliding test conditions

Sliding tests are performed using a custom-built tribometer at LaMCoS. A sketch is shown in Fig. 2. On one side an arm holds the pin in contact with the disk surface. On the other side counterweights are used to oppose to the weight of the pin, of its supporting arms and of the different components of the arm itself. The normal load is applied through a leverage effect, after a calibration process. Friction forces are measured at a sampling rate of 1000 Hz using an S-force sensor (SIKA FTCA50) that can measure traction and compression in a range from 1 to 50 N. A TQ-type displacement sensor serves as a lap count thanks to a small indentation made in the rotating disk. The whole is connected to an acquisition central (DEWESOFT) allowing a synchronization of the signals. More details can be found in a previous work [2, 9].

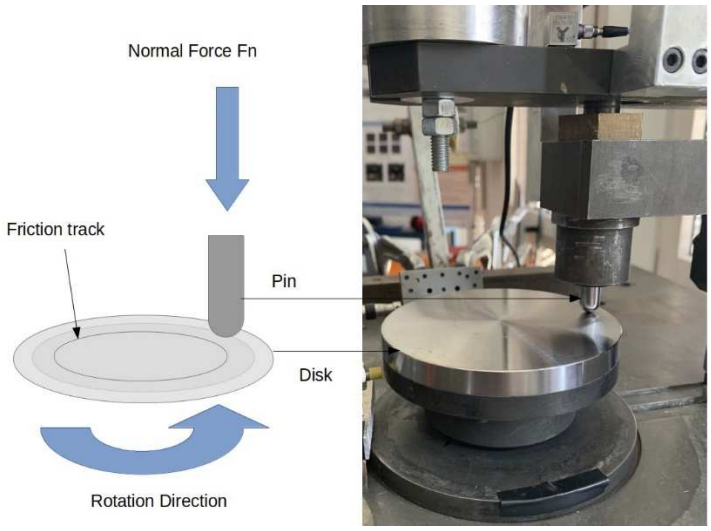

Figure 2: Pin on disk tribometer

Tests are performed in ambient air, at room temperature (27-30◦C). The applied normal force is kept constant, equal to 12.75 N, for all the tests. The calculated maximum Hertzian pressure for the contact geometry corresponds to 1 GPa. The choice of the angular rotation speed coupling with radius of the track (R) leads to a sliding speed of Vlin = 6.28 mm/s for all the tests. For each type of disks, three tests are performed and stopped at different numbers of revolutions: 12.3, 37.5 and 87.0, corresponding to total sliding distances of 3 m, 6 m and 18 m, respectively. Both discs are first tested at a sliding distance of 18 m in order to determine the duration of the running-in phase. 3 m and 6 m are then determined to correspond to the running-in phases.

The table 3 summarizes the experimental conditions of the testing campaign.

Table 3: Summary of tribological experiments

Test number	**Discs**	**R (mm)**	**Angular speed (rpm)**	**Distance (m)**	**Humidity (%)**	**Comments**
1	D//	33	1,82	18	30	Steady state
2	D//	39	1,53	3	27	Running-in phase
3	D//	25,5	2,35	6	27	End of running-in
4	D⊥	33	1,82	18	51	Steady state
5	D⊥	47	1,27	18	51	Steady state
6	D⊥	39	1,53	3	51	Running-in phase
7	D⊥	25,5	2,35	5,5	51	End of running-in

2.3. Approach and strategy

The flow of matter in a sliding system can be described using the tribological circuit (see Fig. 3) [11]. The first bodies in contact, are in relative motion; third bodies form at the sliding interface. The source flow, Q_s, represents detachment of first body material to become the third body; the internal flow Q_i describes the motion of material along the interface; the ejection flow Q_e is material ejected from the interface; the recirculation flow Q_r is ejected material that has been reintroduced to the interface; and the wear flow Q_w is material permanently removed from the sliding system.

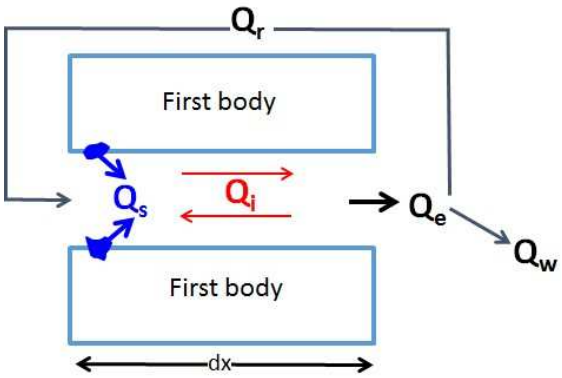

Figure 3: Schematics of the tribological circuit, theoretical for two-dimensional elementary contact (based on Descartes and Berthier, 2002)

Since it cannot be measured, the rheology of the third body is evaluated on the basis of its "cohesion" and its "ductility" [11, 12]. These two properties are determined by observations of the third body (optical and scanning electronic microscopy) and are related to its morphologies and texture, present in most cases in each of the contact conditions at a given scale. The third body can be considered as granular matter and thus cohesion qualification is based on the level of particles compaction. Moreover, this matter flows in the contact and thus ductility qualification is based on the degree of extent of the matter spreading in the contact. Up to now the evaluation of the rheology follows a phenomenological procedure where a chart is necessarily built to produce the qualitative scales for cohesion and ductility. In order to set up a methodology to quantify those characteristics, the following approach is proposed:

Post-mortem analyses of the contact zones of the disk and the pin surfaces are carried out after carefully opening the contact at the end of each test. Observations are made using different tools: optical microscope, optical profilometer (with the Altimet non-contact optical profiler), scanning electron microscopes (SEM, FEI Quanta 600 and Thermofischer Quattro) coupled with Energy Dispersion X-ray analysis (EDX, Oxford Instruments).

When observing the discs, the wear track width is of the order of the millimeter. The table 4 shows the SEM conditions:

Table 4: SEM image acquisition conditions

SEM parameters	**Value**
Scanning velocity (µs)	30
Resolution (px)	1024 x 884
Working distance (mm)	10
High voltage (kV)	20
Spot size	5 (i.e. beam current = 1.2 nA)

The entire track width is traversed to check if it has a regular appearance and then several images are taken at different scales in a 'regular' area (generally at the level of the lap count mark) and if necessary, in an area with an atypical character. There are twelve to fifteen images per track and per pin.

In the present ball-on-flat sliding system, third bodies are formed in the contact. After opening, third body is observed in the wear track and as transfer film adhering to the pin (see Fig. 4). The ejection flow occurs as material is pushed to the sides of the wear track, leading to ejected particles found at the outer edges of the track (blue area in Fig 4). This material becomes wear flow unless it somehow recirculates into the contact, for instance as the wear track widens. The particles in the center of the contact (red area in Fig. 4) highlight an internal flow and a recirculation

flow Q_r. The particles are left in their last location on the contacting surface in order to disturb as little as possible their arrangement, during the opening of the contact. Through this approach the evolution of the contact can be reconstructed.

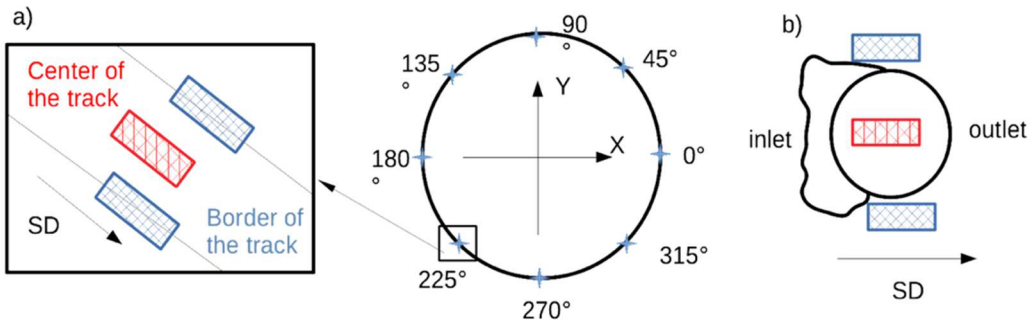

Figure 4: Schematics of the localization of region of interest (ROI) –(a) Disk, (b) Pin

The worn surfaces of the first bodies are systematically submitted to microscopic observation in order to extract morphological and texture characteristics of the third body. The morphological characteristics of the particles describe any information regarding the shape and the aspect of the third body as observed after opening the contact and observing it at the micrometric scale. Thus, the work presented here focuses on an experimental tribological campaign combined with comprehensive SEM observation of the worn surfaces and image processing - image analysis.

3. Friction results

Fig. 5 shows the time series of the tangential force for the tests.

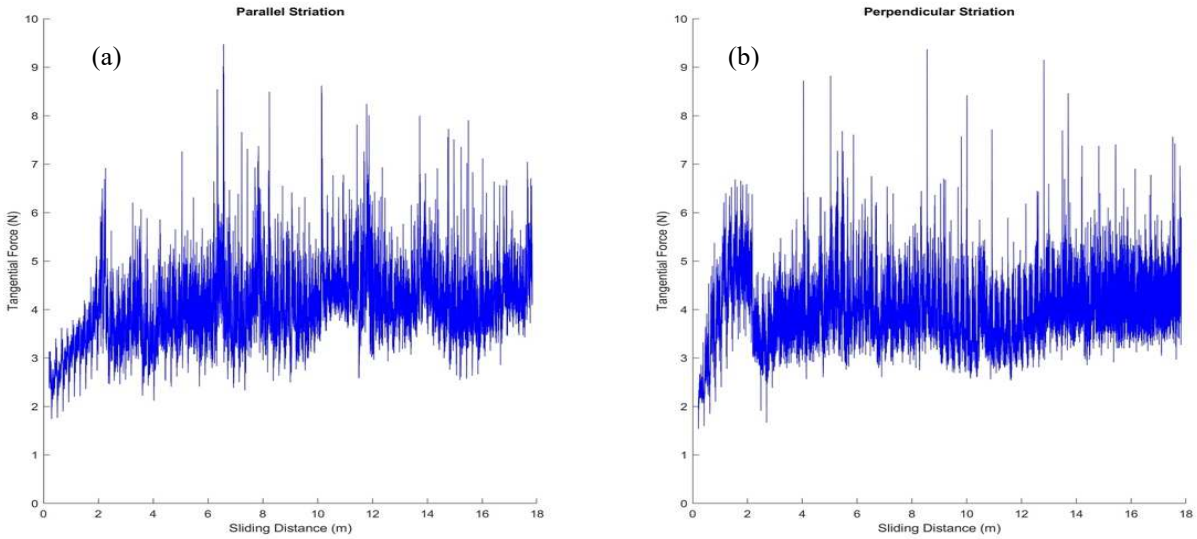

Figure 5: Evolution of the tangential force over time, (a) Disc D// (test 1), (b) Disc D⊥ (test 4)

It is possible to evaluate the average friction factor per lap knowing the normal force applied:

$$Friction\ Factor\ = \frac{Tangential\ force}{Normal\ force}$$

It provides the discrete series shown in Fig. 6.

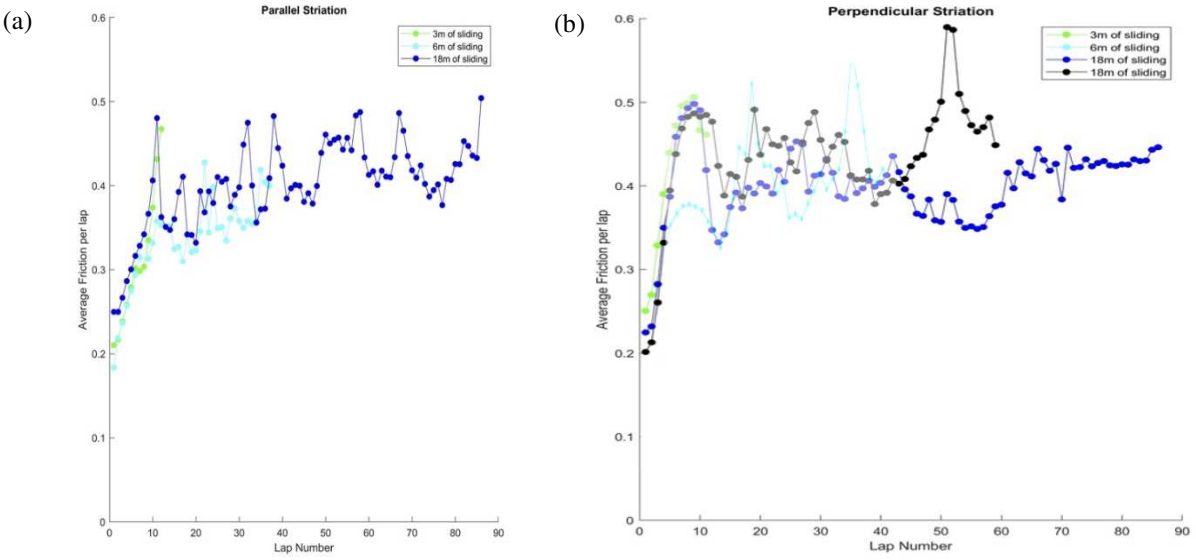

Figure 6: Evolution of the average COF, (a) Disc D//, (b) Disc D⊥

In Fig. 6b, the curve, at 18 m of sliding (test 5), shows a sharp peak at cycle 50. Following the analysis made in [9], the hypothesis is that the peaks could correspond to clusters of third body passing under the pin.

4. Contact's life

4.1. Parallel striations disk D//

It is then possible to observe the third body on the disc. This is the state of third body produced during the last laps.

4.1.1 Running-in phase with parallel striations

In order to complete the contact history, it is necessary to study the third body produced during the running-in phase, tests 3 and 7 (table 3). The observation of the disk D// for Test 3 (Fig. 7) highlights a significant production of ejected particles in the form of clusters. In the center of the track, it is the beginning of the layering of mildly cohesive third body. These overlays do not yet take place all along the runway but rather by small patches.

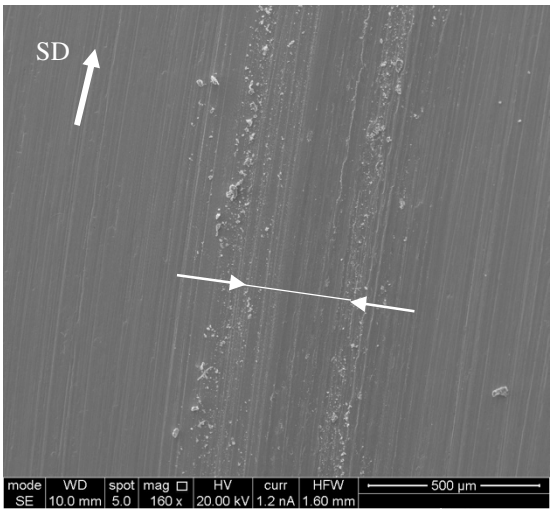

Figure 7: Secondary Electron (SE) image of disk D// (test 3) - (SD: sliding direction)

The surface of the pin 3 has a very high concentration of third body at the inlet (Fig. 8). This third body is in the form of cohesionless clusters whose composition differ across the inlet area. At the farthest from the inner area, the agglomerate is composed of large platelets; the closer one gets to the contact center, the smaller the constituent particles of the cluster. These particles are similar to flakes. In the internal zone, there is a smooth thickness of spread out third body.

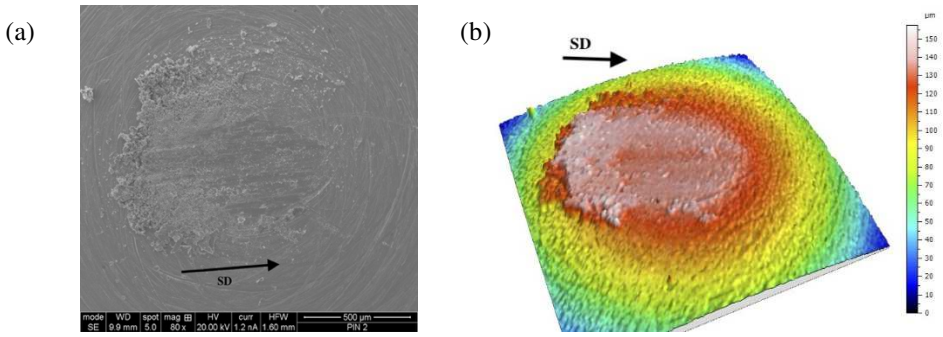

Figure 8: Pin, Test 3 (D//, 6m) – (a) SE image, (b) 3D Profile.

These observations are supported by profilometry and spectroscopic analyses. As for Test 4, the smooth-looking textures seem to come from a mixture of particles crushed on the pawn. An example is shown in Fig. 9. The texture looks very smooth and third body appears compact when observed with the secondary electron (SE) detector. Inversely it is worth noticing that the back scattered electron (BSE) image of the same area highlights individual constituents of this third body with variable mean chemical composition. That means the mixing is not complete, not uniform. Consequently, this observation states that more than one parameter, is necessary to describe the evolution of the interface.

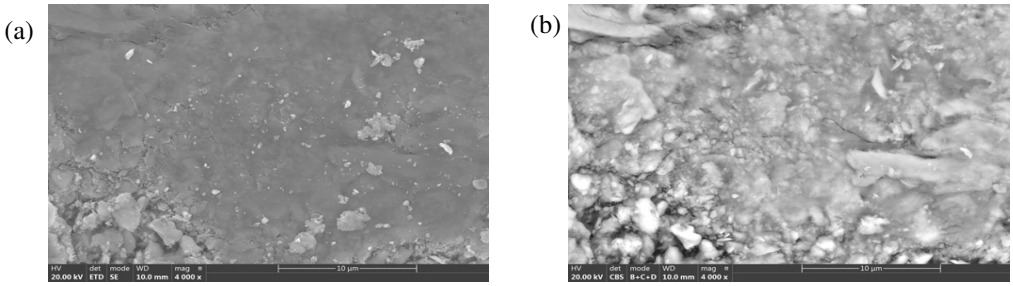

Figure 9: Smooth texture on Pin 3 – (a) SE image, (b) BSE image (contrast linked with mean atomic number of the constituents in the analyzed area) highlighting an agglomerate of particles

4.1.2 Established phase with parallel striations

Test 1 is corresponding to the steady state.

The width of track follows a quadratic trend from 0.11 mm to 0.40 mm +/- 0.1 mm during the running-in phase before reaching 1.29 ± 0.1mm (Fig. 10). The third body observed in the center of the track is mildly cohesive, thicknesses are superimposed and spread out (crushed) without being smoothed. The wear flow, corresponding to the ejected particles, is composed of particle clusters.

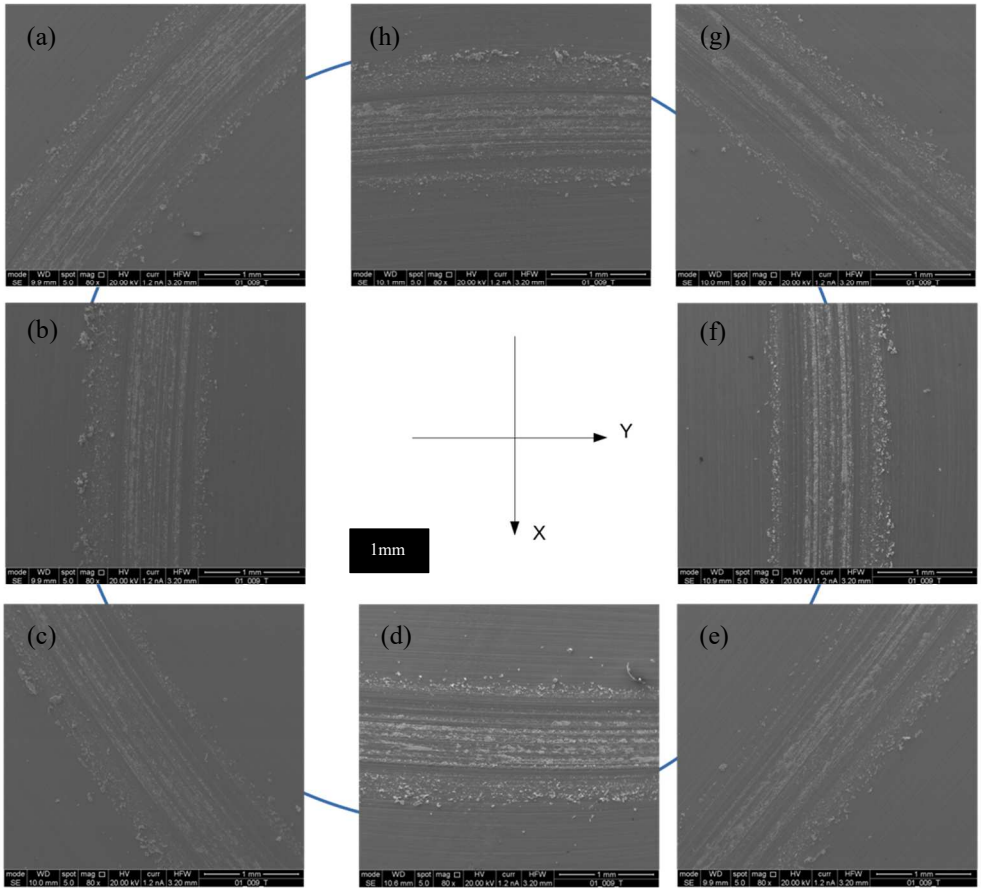

Figure 10: SE image of disk D// after 18 m of sliding (a) position 1, (b) position 2, (c) position 3, (d) position 4, (e) position 5, (f) position 6, (g) position 7 and (h) position 8

When studying the track of the D// disc, the concentration of the third body ejected outside the track is greater than inside. Moreover, the third body at inner border of track seems bigger, or more agglomerated. This observation is independent of the position on the track.

These observations can be completed by studying the pin (Fig. 11). The combination of SEM image and profiles views provides additional information.

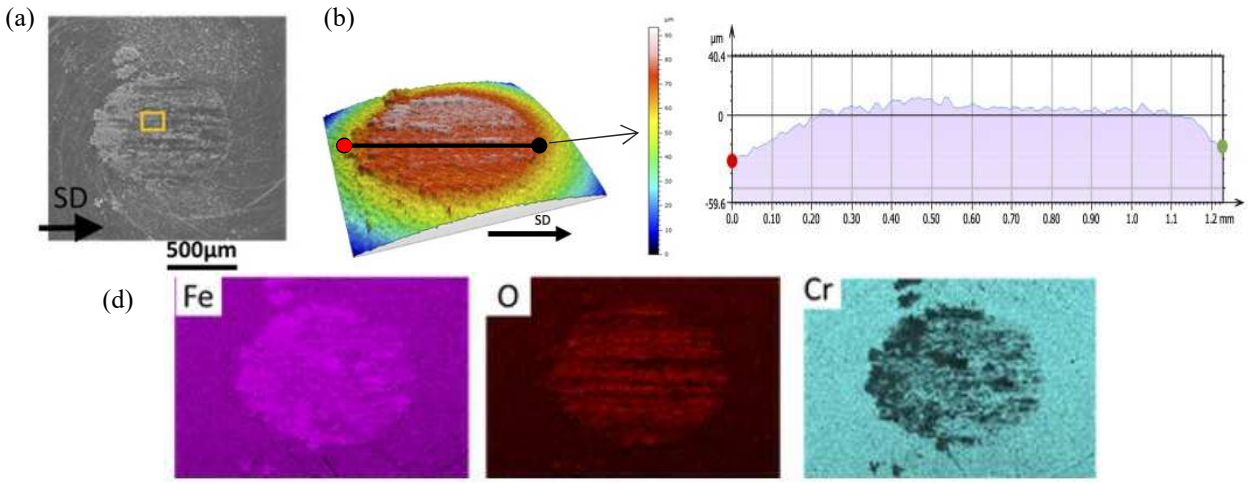

Figure 11: Pin, Test 1 (D//, 18m) – (a) SE image, (b) 3D Profile, (c) Longitudinal extracted 2D Profile, (d) EDX mapping

The third body observed on the pin has characteristics similar to that of the disc. That is a third body not very cohesive (“pulverulent”) at the contact inlet (Fig. 12a), with ejection of clusters more or less large in the lateral zones. In the center part of the contact third body is smoother, indicated it has been compacted and spread. Smooth areas, highlighted in the center (Fig. 12b) can be interpreted as areas of greater contact pressure.

As in the running-in phase, the third body on the pin, at the center of the contact is smooth (Fig. 9a and Fig. 13a). However, observation using the BSE detector provides additional information on the chemical composition of this third body. The mixing process started during the running-in phase (Fig. 9b) and homogenized in a steady state (Fig. 13b).

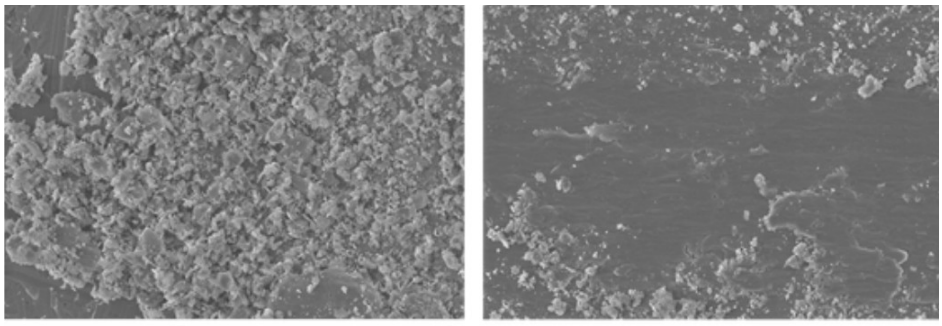

Figure 12: Third body morphology on the pin, (a) pulverulent at the inlet (b) cohesive in the center

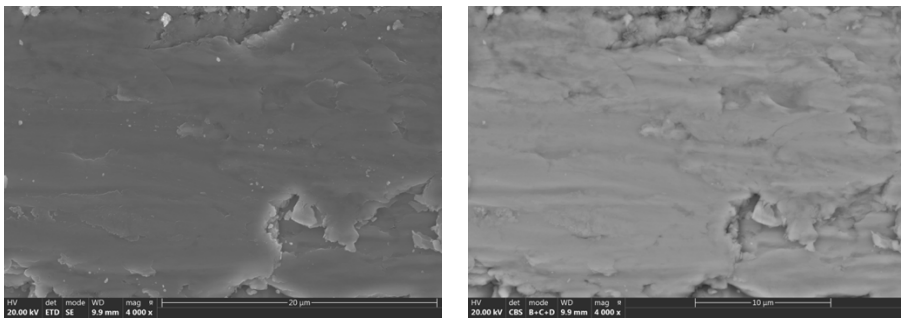

(a) (b)

Figure 13: Smooth third body in center of contact, on the pin – (a) SE image, (b) BSE image

It is then very helpful to observe its chemical composition through spectroscopy. Areas of third body with little cohesiveness show a higher oxygen concentration (Fig. 14). It is possible to assume that the particles of the powdery areas have been more exposed to oxygen and consequently are oxidized, as opposed to the constituents of the third body of smoother areas. A highly compacted third body, related to a very smooth texture on surface, tends to be much less porous. Therefore, less oxygen diffuses in this compacted third body, on the contrary of the powdery third body. That may explain the oxidation difference. And this is closely linked to third body flows. The works of Baydoum et al. [13], Zhang et al. [14] or Shockley et al. [15] tend to corroborate this hypothesis.

The other information from the pin study comes from the extraction of a 2D profile in the friction direction. (Fig. 11c). The profile shows a planar face indicating that the pin has worn out. The steep slope at the green point confirms the presence of an accumulation of third body at the contact inlet, accumulation observed on the Fig. 11a, b.

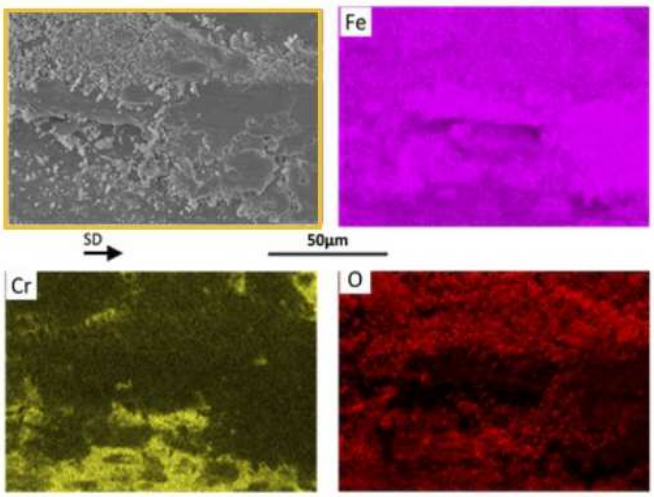

Figure 14: Pin, Test 1 (D//, 18m) – Se image and EDX Mapping

4.2. Perpendicular striations disk D⊥

4.2.1 Running-in phase

On the disk D⊥, there are little ejected particles along the friction track (Fig. 15a), the borders of the track are smooth (Fig. 15b). In its center, two textures coexist, a smooth texture and small clusters of crushed cohesionless third body.

On the pin, the third body is powdery in the center and at the inlet of the contact. The SEM image on the pin shows also very smooth areas on both sides of the track.

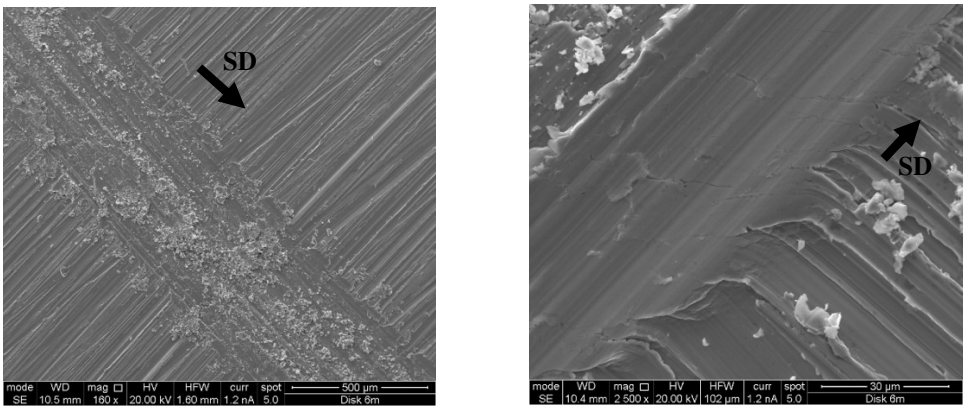

Figure 15: Disk D⊥ (6m of sliding) SE image (a) Track, (b) Border of the track

(a)

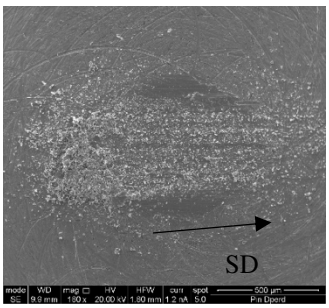

(b)

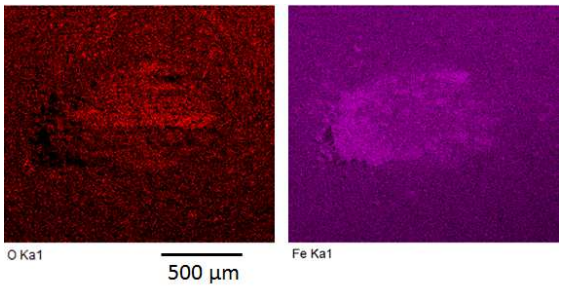

Figure 16: Pin, Test 7 (D⊥, 6 m) – (a) SE image, (b) EDX mapping

4.2.2 Established phase with perpendicular striations

Like D//, the width of track follows a quadratic trend from 0.08 mm to 0.18 mm during the running-in phase before reaching 1.09 ± 0.1 mm.

The disk (D⊥) has an overall texture similar to disk (D//) to some exceptions, the ejected particles tend to form fewer clusters but larger “elementary” particles; it is possible to observe smooth areas on the track. The observation of the entire track highlights a different production of ejected particles than in the case of D//. Actually, there is a higher production of particles outside the runway (Fig. 10), while the production seems more important inside (Fig. 17). However, this distribution is reversed all along the track, alternating between areas of strong internal and external ejection.

Inside the track, cluster of particles have been compacted and spread on the surface.

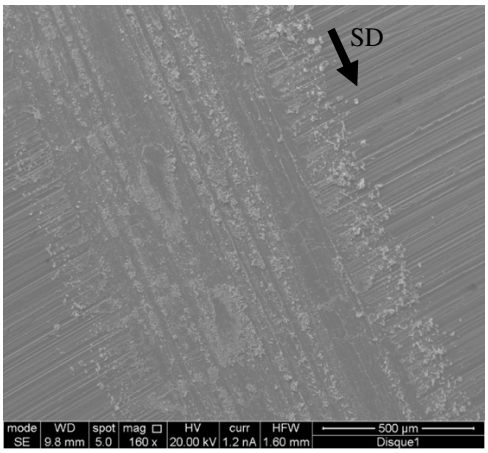

Figure 17: Disk D⊥ (18m of sliding) SE image

The pin has a high concentration of third body, which is not very cohesive in the inlet. In lateral zones little ejection of clusters, and isolated particles, are observed. The inner zone has a very smooth central band, indicating a significant pressure. The profilometry study of the pin makes it possible to observe a planar area, indicating substantial wear of the pin and a large third body agglomeration at the inlet (red dot in Fig. 18c).

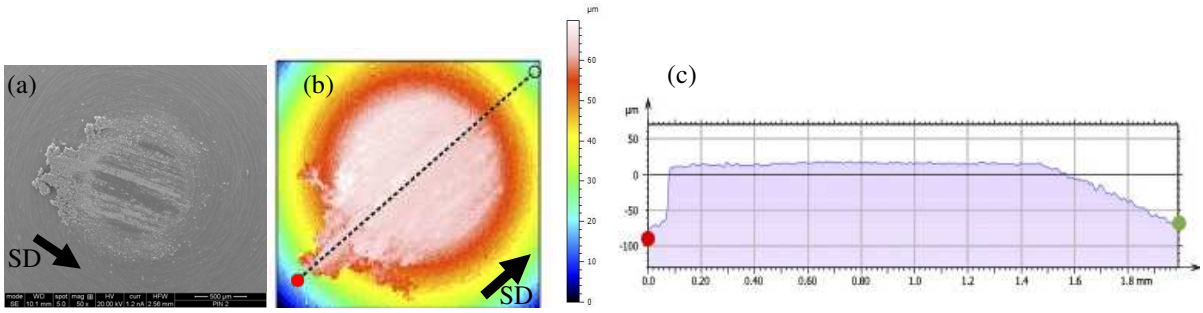

Figure 18: Pin, Test 4 (D⊥, 18 m) – (a) SE image, (b) 3D Profile, (c) 2D profile following sliding track

4.3. Synthesis

The qualitative study of the two configurations suggests that in the established regime the behavior of the third body, while not identical, is very similar. The wear flow is composed of many particles, individual or in the form of agglomerates, and the recirculation flow forms little non cohesive and crushed layers in the tracks center. The same goes for the corresponding pins with a more important agglomeration of third body at the contact inlet for D⊥ than D// case.

The major differences between D// and D⊥ will occur in the running-in phase. Unlike the disk D//, there is no production of ejected particles in the case of disk D⊥. Moreover, the observation of the track center suggests that the mechanisms leading to the stationary state are not the same. Indeed, with the disk D// the third body begins to be created from the pin, creating a planar surface of moderate extension, and depositing on the track in the form of mildly cohesive clumps which will superimpose and be crushed at the passage of the pin. While in the case of the disk D⊥, with equivalent distance travelled, there is creation of large cohesionless clusters, but they do not seem to come from the pin but rather from the disk. These clusters coexist with smoothed areas that are unlikely to have undergone oxidation, suggesting that the striations have plasticized as the pin passed and then were eventually torn off after a certain time creating the textures observed in the stationary regime.

In order to measure to what extent the third body descriptions are similar or not, and to analyze its evolution, quantification of third body characteristics is carried out. The wear flow study is based on calculation of the morphological properties of the third body particles ejected on the edge of the friction track. While the study of the texture of the third body in the center of the track provides information on the internal flow, or recirculation flow.

5. Quantification

In order to go beyond the qualitative study of the contact, the morphological and texture properties of the third body will be calculated. Image processing will be used as quantification tool.

5.1. Morphological, geometrical and topological characteristics – wear flow

To extract the geometrical, morphological and topological characteristics [16, 17, 18, 19], the particles of third body, constituent of the ejection flow, are first analyzed. The images of the particles are taken at the edge of the friction strip, on the lateral border of the track on the disk. These images are segmented thanks to a program developed in python 3.6, whose overall functioning is shown in Fig.19.

This program is interactive and asks the user to make choices at each step, such as selecting a filter after presenting the possibilities, or a change in the exposure. Once the changes are made the image is binarized by Otsu thresholding [20] and then cleaned.

As mentioned in the previous section, it may happen that some particles have textures that do not allow segmentation by thresholding. This is the case for powder-like third body, for which the darker areas on their surfaces could be interpreted as holes by Otsu's thresholding, an example of this problem is illustrated on Fig.20. To solve this issue, another python code using machine learning algorithms was developed to segment the images.

The operation of this program is shown in Fig. 19 (orange rectangle on the right, i.e. "ML"). First, the user chooses a particle image whose pixels serve as the input base for machine learning. This particle is manually segmented by the user in order to create the labels "belongs" or "does not belong" to the particle, affected to each pixel. In a second time features are extracted in this training image, such as morphological profiles and profiles of texture [1]. Finally, the intelligent algorithm is trained on these extracted characteristics. It is then possible to segment new images with textures similar to the training particle.

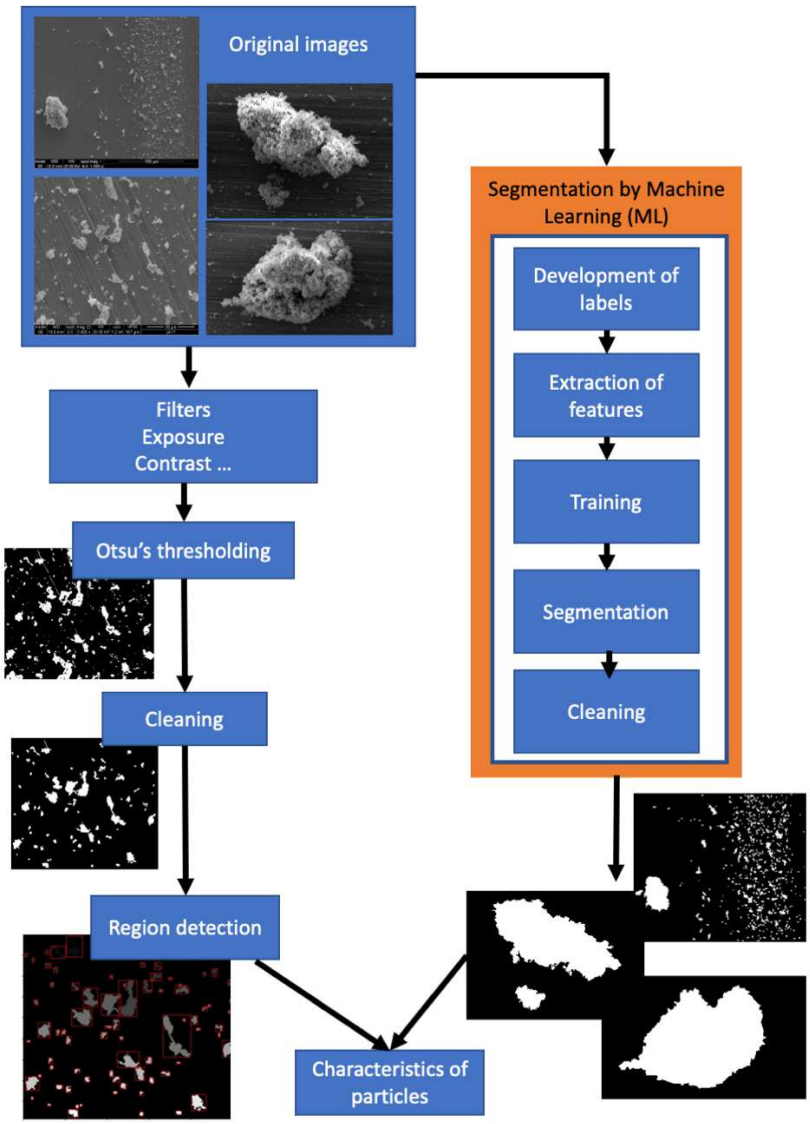

Figure 19: Image Processing steps. Initially, segmentation by thresholding will be preferred. Thanks to the filtering and cleaning operations the results will be very satisfactory in most cases. For complex texture particles, if the user feels that the result is not satisfactory (as shown in Fig. 20), ML segmentation (orange) is required.

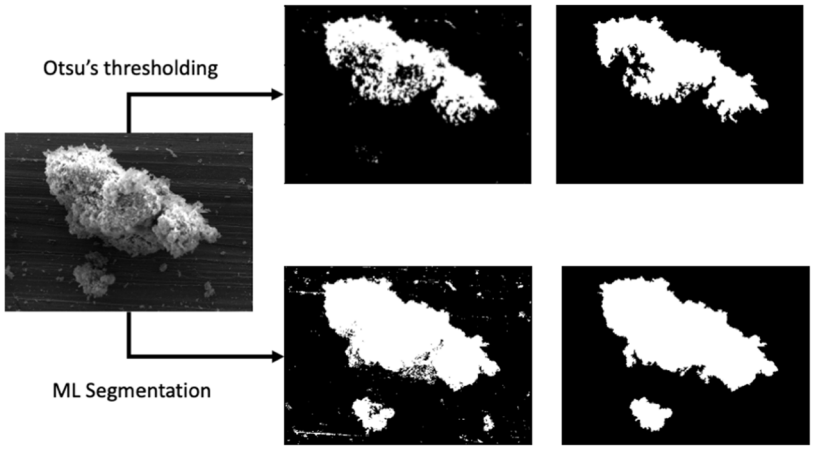

Figure 20: Particle with a texture that does not allow segmentation by Otsu's thresholding. To solve this problem ML segmentation is used.

On the bottom image of the Fig. 19, the machine learning model has managed for example to properly segment the two complex particles or the other one (no holes appear). The use of these two segmentation methods (Otsu thresholding and machine learning) allows to obtain binary images from which the morphological characteristics of each region representing a wear particle can be extracted. A final program that detects the regions present on the binary image and extract certain properties is used:

- Perimeter
- Area
- Convex Area
- Circularity $C = \frac{4\pi\ Area}{Perimeter^2}$
- Elongation $P = \frac{Minor\ axis\ length}{Major\ axis\ length}$

The comparison of the morphological characteristics of the particles, from the two disks, has been done only quantitatively during the steady-state phase. Indeed, the production of ejected particles during the running-in phase for the disc with streaks perpendicular to the pin (disk D⊥) is not sufficient to allow relevant statistical results. Furthermore, the feature extraction focuses on the study of the discs, that allows to visualize the behavior of the contact on a complete cycle (the last one). On the contrary the study of the features of the pin would highlight the moment when the test is stopped and the contact is open.

Thus, the morphological characteristics of the wear particles produced during the steady-state tests for the two discs are extracted and studied. There are 16 areas of interest per disc, two per positions shown in, inside and outside the track (Fig. 4). This represents an average of 65 particles per image. In both cases (D// and D⊥) the particles have similar shape characteristics. The ejected particles of both discs have an average elongation of 0.60 ± 0.02, as well as a very close circularity of 0.49 ± 0.01 for D// and 0.38 ± 0.01 for D⊥. Similarly, for size characteristics, the average area of third-body particles is 182 µm2 for D// and 172 µm2 for D⊥.

However, it is important to note that the influence of image acquisition parameters may be significant. Indeed, an overexposed image would induce errors when extracting characteristics up to 10%. An overexposure could be characterized by the saturation of part of the image and thus leads to loss of information. For example, some close particles could be assimilated to a single large particle: the number of analyzed particles being decreased, the resulting perimeter is inaccurate, as well as all the characteristics that result from it. Therefore, the contrast and brightness must be carefully adjusted during images acquisition.

5.2. Textures - recirculation / internal flow

Looking at images in the center of contact (red area in Fig. 4), it appears that the third body is spread out and therefore does not allow a segmentation study. This is why the choice to use the co-occurrence matrix as a texture study tool [21, 22, 23] is made. This matrix counts neighboring pixel pairs in terms of intensity at a given angle and distance, one matrix per couple of angle and distance (Fig. 21).

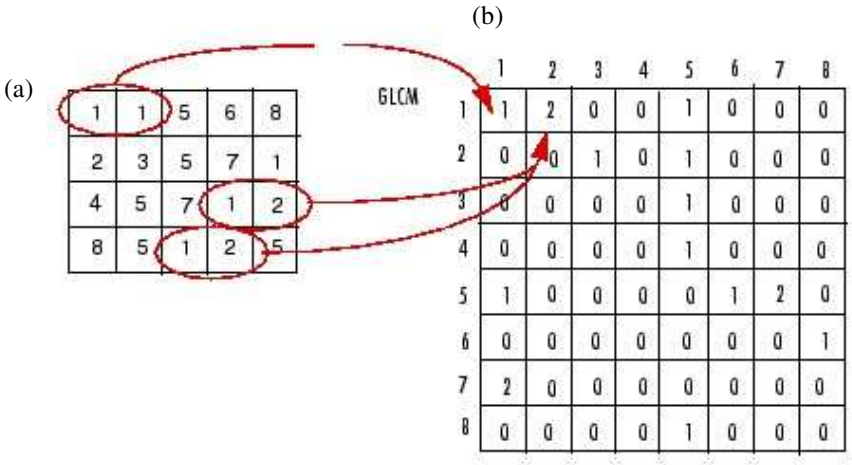

Figure 21: Illustration of co-occurrence matrices construction. (a) Matrix representation of grayscale image I size 5x5 with gray level 1 to 8, (b) Co-occurrence matrix $M_{1,0}$ size 8x8 where the entries m(i,j) indicates the number of occurrences of gray values i and j being a neighbor with distance d = 1 in the direction of 0° in the matrix I.[24]

This matrix is calculated on selected areas of interest on third body images, then its properties are calculated. These quantities are Contrast, Dissimilarity, Homogeneity, Energy, Correlation and Entropy [23]. Only entropy is chosen as a first step. This choice is not trivial but determined by the future studies to carry out, as elaborated below. Indeed, entropy is a parameter that has proven to be very discriminating when studying the classification of wear particles using neural networks [21]. But also, because it is possible to give it a physical meaning in the sense of information theory. It is calculated as follows:

$$Entropy = -\sum_{i=0}^{L-1} p(z_i) log_2 p(z_i)$$

These co-occurrence matrices are calculated for three distances and four angles, which provides 12 values for each calculated characteristic. It is important to note that this work is made with images in bitmap format, coded on 8 bits, this choice is justified because 8bits images present a sufficient resolution and 256 gray levels. This results in co-occurrence matrices of dimensions (256 x 256).

Therefore, a selected region of interest (ROI) is extracted in the central area of the friction track of each disc for the three phases, making sure to be on the same scale on each image. Then the co-occurrence matrices and the resulting characteristics are computed.

The entropy is lower in the case of disk D⊥ compared to disk D// at middle of the running-in phase (Fig. 22, phase 1). This is due to the fact that the same pairs of pixels are often found, which can result in a smoother texture. Indeed the striations parallel to the track (disc D//) allow a higher production of wear particles during this phase. Whereas, in the case of D⊥, there is little or no production of third body and striations seem flattened and plasticized.

In both cases, the entropy increases with the distance travelled (comparison phase 1 and phase 2 results). During the running-in phase, there is an important production of particles, but with less ejection for D⊥ contrary to D// (which would end up being crushed and ejected in steady-state). As an example, the two images of D⊥ (bottom of Fig. 22) highlight track's evolution in ROI A. Furthermore, for a same disc, the value of entropy at the same phase varies

function of the ROI. This is a “random effect” due to the selection of ROI. Indeed, the production of particles seems irregular along a same turn and the density of particles differs.

The differences between D// and D⊥ observed during the running-in phase are becoming increasingly blurred once the steady state is reached (phase 3). Entropy is then of similar values for both disks. Furthermore, entropy values are lower than the ones in the middle of the running-in. Work of Jaza et al. [2] showed the friction curves were not perfectly superimposed when changing only the sliding distance parameter. In particular, some friction peaks were present during tests. Those were due to clusters of third body that passed periodically under the pin [9], thus the particles agglomerates are compacted and spread on the surface. As a consequence the surface would become smoother. Thus the result can be potentially influenced if the test is stopped when this type of event occurs during the last turn. The particles produced during running-in phase seem to be less numerous or smoother. They could have been spread on the track, but also ejected from the contact; coupling with the random selection of ROI, exposed previously, it can explain the lower values of the entropy in phase 3.

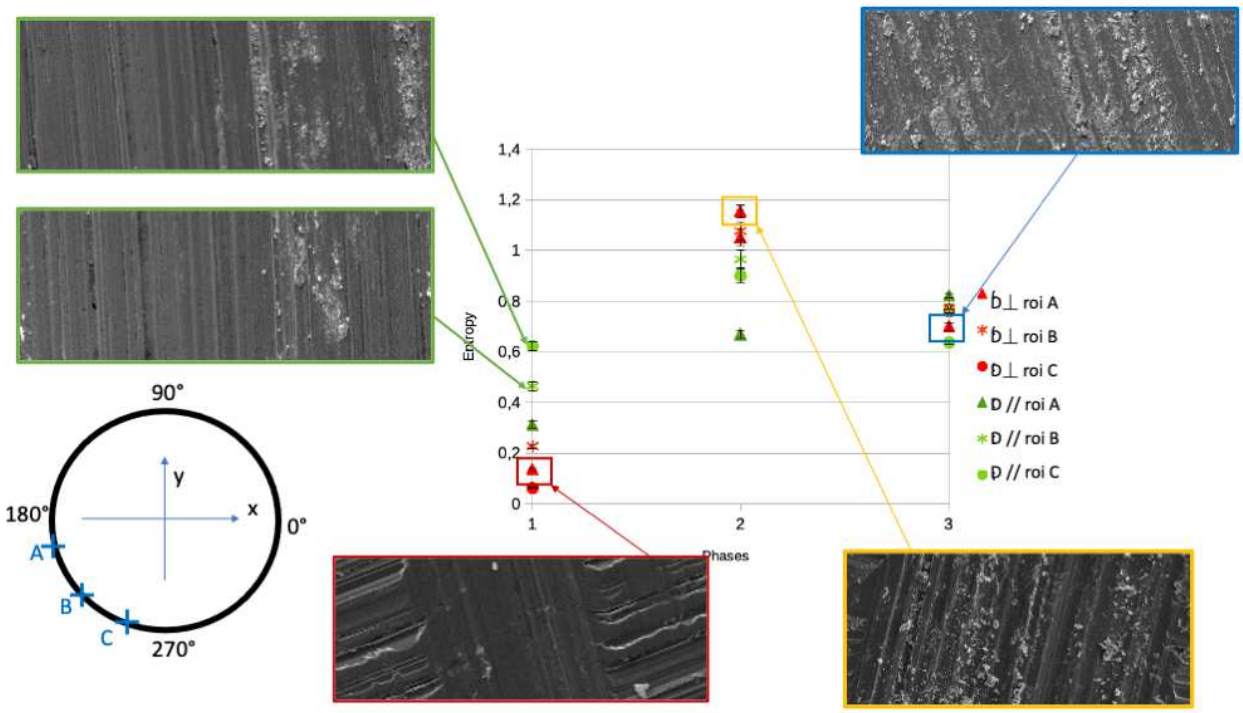

Figure 22: Evolution of entropy with sliding distance

5.3. Synthesis

The quantitative approach confirms the observations made in the previous section. Although not identical, the ejected third body has very similar geometric and morphological characteristics for the two discs, with variations not exceeding 20%. However, it is important to note that these observations are made on average values, the observation of tracks sections in section 4 makes it possible to detect different trends from one disk to another. For example, the number of particles per image, the average values are 71.5 for D// and 62.3 for D⊥, these values are quite close, however their distribution on the disks are not the same. For the D// disc there are more particles on the outer edge of the track while for D⊥ there is a trend reversal (more particles inside from 0 to 180°and then outside from 180 to

360°).

This type of phenomenon is found for all the parameters studied but tends to compensate on the full cycle, which makes it possible to observe similar trends from one disc to another. These phenomena can be explained by the passage of a cluster of third bodies and will be the subject of a future study based on accelerometer data and *in situ* analysis to confirm this possible origin.

The other important point of this quantitative study is the study of texture. The study with the co-occurrence matrix alone, especially entropy, provides relevant information but not sufficient to establish reliable conclusions. The data need to be supplemented by other texture descriptors in order to validate or invalidate the hypotheses made on the life of the contact.

Recall that the entropy, as it is defined here, allows to give an indication of the disorder, that is the presence of third body, not smoothed or little, in the center of track. Others relevant features of the co-occurrence matrix, such as contrast, homogeneity or inertia, will be studied in subsequent studies to complement this first-line study. Although obvious links with the rheological data are not so straightforward, others descriptors will also be added to those, such as statistics on histograms in gray shade. Finally, it will allow to characterize the texture more accurately and fully. The combination of these descriptors would give indications on the evolution of the recirculation flow of third body.

The diversity of third body structures and their complexity requires the search for relevant descriptors of both morphology and texture. Their importance for future machine learning work should not be overlooked as they may represent a significant learning parameter [21].

6. Conclusion

During these tests, the goal was to study the influence of the surface condition of one of the first bodies on the morphology of the third body, at several stages of the contact's life (middle of running-in, end of running-in and stationary regime). It emerges that in those cases the surface condition have little influence on the morphology of the particles ejected in established regime. Indeed, they appear to be of similar shape while only the size seems to vary according to the initial surface. The most significant difference is in the running-in phase. The striations parallel to the friction track tend to allow a more important production of wear particles than with perpendicular striations. This is why the study of the texture of the third body trapped in the contact is used.

Initially qualitatively described with observations of the pins and discs, the third body is quantitatively characterized with image processing in a second step. This qualitative approach is supported by the calculation of co-occurrence matrices, especially one of the resulting characteristic, the entropy (among others). It allows to quantify the disorder in the texture. Especially in the case of disk $D_{\perp}$, an increase in entropy is observed until reaching a similar level in both cases. On the basis on these observations, we can therefore say that the initial surface condition of the disc (first body) only have an influence during the running-in phase of the dry friction tests. At the steady state the two discs behave in a similar manner, the production of third body providing ejected particles of similar shapes and a third body in the center of a relatively close texture track.

However, we were confronted with a well-known dilemma of the tribologists, namely the dilemma of "agglomerates". From what size an agglomerate is considered as a particle? Can an agglomerate be considered as a large particle or is it an object as such? To temporarily compensate for it, a study distance allowing to assimilate the agglomerates to large particles is chosen. On the other hand, when the particles agglomerate to a large powdery mass, it is

necessary to study the texture obtained in its entirety, as in the center of the track.

Another important point is the special care that is needed in the acquisition of images. A fuzzy or poorly exposed image leads to a loss of information. A contrast defect is less annoying because of the use of machine learning segmentation program, based on contrast-independent image characteristics.

In the future, it will be interesting to get rid of the subjectivity of the user during the segmentation. Thus it is envisaged to work with convolutive networks of type U-net. The longer-term goal will be to use machine learning algorithms to link rheological characteristics, such as the coefficient of friction, with the morphological characteristics of different types of third body produced, without needing to isolate particles during image processing.

Acknowledgements

This work was carried out thanks to the financial support of Manutech-SLEIGHT ANR-17-EURE-0026, IDEXLYON of Université de Lyon in the framework of the French National Program "Investissement d'Avenir" (ANR-16-IDEX-0005).

CRediT statements

Alizée Bouchot: Investigation, Software, Methodology, Writing-original draft.
Amandine Paquet: Technical support
Guilhem Mollon: Supervision, Conceptualization, Review & editing.
Johan Debayle: Supervision, Conceptualization, Review & editing.
Sylvie Descartes: Supervision, Conceptualization, Writing - review & editing, Funding acquisition.

7. References

[1] T. Ojala, M. Pietikainen, and T. Maenpaa. Multiresolution gray-scale and rotation invariant texture classification with local binary patterns. IEEE Transactions on Pattern Analysis and Machine Intelligence, 24(7):971–987, 2002.
[2] R. Jaza and al. Lessons learned using machine learning to link third body particles morphology to interface rheology. Tribology International 153 (2021) 106630.
[3] Y.-W. Chung and Q. J. Wang. Encyclopedia of tribology: With 3650 Figures and 493 Tables. Springer, 2013.
[4] M. Godet. The third-body approach: a mechanical view of wear. Wear, 100(1-3):437–452, 1984.
[5] Y. Berthier. Maurice godet's third body. In D. Dowson, C.M. Taylor, T.H.C. Childs, G. Dal- maz, Y. Berthier, L. Flamand, J.-M. Georges, and A.A. Lubrecht, editors, The Third Body Concept Interpretation of Tribological Phenomena, volume 31 of Tribology Series, pages 21 – 30. Elsevier, 1996.
[6] A. D.H. Thomas, T. Davies, and A. R. Luxmoore. Computer image analysis for identification of wear particles. Wear, 142(2):213–226, 1991.
[7] B. J. Roylance and S. Raadnui. The morphological attributes of wear particles - their role in identifying wear mechanisms. Wear, 175(1-2):115–121, 1994.
[8] C. Kowandy, C. Richard, and Y. M. Chen. Characterization of wear particles for comprehension of wear mechanisms. Case of PTFE against cast iron. Wear, 265(11-12):1714–1719, 2008.
[9] R. Jaza, G. Mollon, S. Descartes, A. Paquet, and Y. Berthier. Relating the morphological description of the third body to its rheological behaviour. Journées internationales francophones de Tribologie, JIFT2019, Tours, presse des Mines, 2019, 6 pages, in English.
[10] Z. Peng and T. B. Kirk. Automatic wear-particle classification using neural networks. Tribology Letters, 5(4):249–257, 1998.
[11] S. Descartes and Y. Berthier. Rheology and flows of solid third bodies: background and application to an $MoS_{1.6}$ coating. Wear, 252(7-8):546–556, 2002.
[12] S. Descartes, C. Godeau, and Y. Berthier. Friction and lifetime of a contact lubricated by a solid third body formed from an mos1. 6 coating at low temperature. Wear, 330:478–489, 2015.
[13] S. Baydoun and S. Fouvry. An experimental investigation of adhesive wear extension in fretting interface: Application of the contact oxygenation concept. Tribology International, 147:106266, 2020.

[14] Y. Zhang, G. Mollon, and S. Descartes. Significance of third body rheology in friction at a dry sliding interface observed by a multibody meshfree model: Influence of cohesion between particles. Tribology International, 145:106188, 2020.
[15] J. M. Shockley, EF Rauch, RR Chromik, and S. Descartes. TEM microanalysis of interfacial structures after dry sliding of cold sprayed Al-Al_2O_3. Wear, 376:1411–1417, 2017.
[16] J. Debayle. Geometrical and morphometrical tools for the inclusion analysis of metallic alloys. Metallurgical Research & Technology, 116(5):508, 2019.
[17] S. Rivollier, J. Debayle, and J.-C Pinoli. Shape diagrams for 2d compact sets-part i: analytic convex sets. Article, 2:1–27, 01 2010.
[18] S. Rivollier, J. Debayle, and J.-C Pinoli. Shape diagrams for 2d compact sets-part ii: analytic simply connected sets. The Australian Journal of Mathematical Analysis and Applications [electronic only], 7, 01 2010.
[19] S. Rivollier, J. Debayle, and J.-C Pinoli. Shape diagrams for 2d compact sets. iii: Convexity discrimination for analytic and discretized simply connected sets. The Australian Journal of Mathematical Analysis and Applications [electronic only], 7, 01 2010.
[20] N. Otsu. A threshold selection method from gray-level histograms. IEEE Transactions on Systems, Man, and Cybernetics, 9(1):62–66, 1979.
[21] A. K. Muhamad and F. Deravi. Neural networks for the classification of image texture. Engineering Applications of Artificial Intelligence, 7(4):381–393, 1994.
[22] R. M. Haralick, K. Shanmugam, and I. Dinstein. Textural features for image classification. IEEE Transactions on Systems, Man, and Cybernetics, SMC-3(6):610–621, 1973.
[23] Laleh Armi and Shervan Fekri-Ershad. Texture image analysis and texture classification methods - a review, 2019.
[24] A. F. Oeoen, S. Madenda, E. Ernastuti, and D. Kerami. Wood texture features extraction by using glcm combined with various edge detection methods. Journal of Physics: Conference Series, 725:012005, 06 2016.
